The Astrophysical Journal, 695:59–74, 2009 April 10 doi:10.1088/0004-637X/695/1/59

DETECTING FLARING STRUCTURES IN SAGITTARIUS A* WITH HIGH-FREQUENCY VLBI

Sheperd S. Doeleman[1], Vincent L. Fish[1], Avery E. Broderick[2], Abraham Loeb[3], and Alan E. E. Rogers[1]
[1] 1Massachusetts Institute of Technology, Haystack Observatory, Route 40, Westford, MA 01886, USA
[2] 2Canadian Institute for Theoretical Astrophysics, University of Toronto, 60 St. George St., Toronto, ON, M5S 3H8, Canada
[3] 3Institute for Theory and Computation, Harvard University, Center for Astrophysics, 60 Garden St., Cambridge, MA 02138, USA
Received 2008 July 16; accepted 2009 January 8; published 2009 March 27

ABSTRACT

The super-massive black hole candidate, Sagittarius A*, exhibits variability from radio to X-ray wavelengths on timescales that correspond to < 10 Schwarzschild radii. We survey the potential of millimeter wavelength very long baseline interferometry (VLBI) to detect and constrain time-variable structures that could give rise to such variations, focusing on a model in which an orbiting hot spot is embedded in an accretion disk. Nonimaging algorithms are developed that use interferometric closure quantities to test for periodicity, and applied to an ensemble of hot spot models that sample a range of parameter space. We find that structural periodicity in a wide range of cases can be detected on most potential VLBI arrays using modern VLBI instrumentation. Future enhancements of millimeter/submillimeter VLBI arrays including phased-array processors to aggregate VLBI station collecting area, increased bandwidth recording, and addition of new VLBI sites all significantly aid periodicity detection. The methods described herein can be applied to other models of Sagittarius A*, including jet outflows and magnetohydrodynamic accretion simulations.

Key words: accretion, accretion disks – black hole physics – Galaxy: center – submillimeter – techniques: interferometric

Online-only material: color figures

1. INTRODUCTION

Observations of the compact radio/IR/X-ray source Sagittarius A* (Sgr A*) make the most compelling case for the existence of super-massive black holes. Both speckle imaging and adaptive optics work in the near-infrared (NIR) band show that multiple stars orbit the position of Sgr A* (Ghez et al. 2008; Gillessen et al. 2009). These orbits are consistent with a central mass of $\sim 4 \times 10^6\ M_\odot$ contained within 45 AU—the closest approach of any star. Radio interferometric proper motion measurements (Backer & Sramek 1999; Reid & Brunthaler 2004) limit the motion of Sgr A* to < 15 km s^{-1}, implying that Sgr A* must trace at least 10% of the mass determined from stellar orbits. Very long baseline interferometry (VLBI) at 1.3 mm wavelength (Doeleman et al. 2008) has resolved Sgr A*, and measures an intrinsic size of < 0.3 AU (assuming a distance of 8.0 kpc, from Reid 1993), or 4 times the Schwarzschild radius of the central mass ($R_S \approx 10\ \mu$as). Assuming Sgr A* marks the position of the black hole, the implied density, using the proper motion lower limit on the mass and the VLBI size, is $> 9.3 \times 10^5\ M_\odot$ AU^{-3}. Almost any conceivable aggregation of matter would, at this density, quickly collapse to a black hole (Maoz 1998).

The 1.3 mm VLBI result confirms the existence of structures within Sgr A* on size scales commensurate with the innermost accretion region, and matches size scales inferred from light curve monitoring over a broad wavelength range. Sgr A* exhibits variability on timescales of minutes to hours in the radio, millimeter, NIR, and X-ray bands (e.g., Baganoff et al. 2001; Aschenbach et al. 2004; Genzel et al. 2003; Ghez et al. 2004; Bélanger et al. 2006; Meyer et al. 2006; Yusef-Zadeh et al. 2006; Marrone et al. 2006; Hornstein et al. 2007), and flare rise times in the X-ray and NIR correspond to light-crossing times of $< 12\ R_S$. Models that produce flaring X-ray flux density via Synchrotron Self-Compton scattering of IR photons require emission regions of diameter $< 10\ R_S$ (Marrone et al. 2008).

The resolution of millimeter and submillimeter wavelength VLBI is well matched to the scale of inner disk physics. Baselines from Hawaii or Western Europe to Chile provide fringe spacings as small as 30 μas (3 R_S) at 230 GHz and 20 μas at 345 GHz. Millimeter VLBI thus has the potential to detect signatures of hot spot and jet models proposed to explain the rapid variability of Sgr A* as well as strong general relativistic effects, such as the black hole silhouette or shadow (Falcke et al. 2000; Broderick & Loeb 2006b; Huang et al. 2007; Markoff et al. 2007). Extending the VLBI technique to short (0.85 mm, 1.3 mm) wavelengths is essential for this work due to the interstellar scattering toward Sgr A*, which broadens radio images with a λ^2 dependence (Backer 1978). VLBI at 7 mm and 3 mm wavelengths (Rogers et al. 1994; Doeleman et al. 2001; Bower et al. 2004; Shen et al. 2005) limits the intrinsic size of Sgr A* to be < 2 AU and < 1 AU respectively, but VLBI at these wavelengths is strongly influenced by scattering effects. For $\lambda < 1.3$ mm the scattering size is less than the fringe spacings on the longest possible baselines. Recent 1.3 mm VLBI results (Doeleman et al. 2008), coupled with ongoing technical advances to reach 0.85 mm, strongly suggest that it is not a question of *if* but *when* VLBI will directly probe Sgr A* on event horizon scales.

Claims of observed periodicity in IR and X-ray light curves (Bélanger et al. 2006; Meyer et al. 2006; Eckart et al. 2006) during Sgr A* flares, can potentially be explained in the context of hot spots orbiting the black hole at a few times R_S. It has been proposed that the fastest periodicity can be used to constrain the spin of the black hole, since the period of the innermost stable circular orbit (ISCO) is much shorter for a maximally rotating Kerr black hole than for a nonrotating Schwarzschild black hole (Genzel et al. 2003). Indeed, several authors have argued that the black hole must be rotating based on observed

rapid X-ray and infrared periodicities (Aschenbach et al. 2004; Bélanger et al. 2006; Meyer et al. 2006). A recent analysis of the longest (600 minute) NIR light curve to date (Meyer et al. 2008) does not find a statistically significant periodicity, which would result from a single orbiting hot spot, but instead concludes that NIR variations are characterized by a smooth power-law power spectrum. Meyer et al. (2008), however, do not rule out more complex models of inward spiraling hot spots, or flares due to multiple hot spots.

Alternatives to hot spot models include scenarios in which flaring activity is caused by magnetohydrodynamic turbulence along with density fluctuations (Goldston et al. 2005). Rossby wave instabilities may also naturally produce periodicities on the order of tens of minutes, in which case it is not necessary to appeal to a nonzero black hole spin to explain the fast quasi-periodic flares seen at multiple wavelengths (Tagger & Melia 2006; Falanga et al. 2007). We also note that recent estimates of delays between flares in the submillimeter band and those observed in the NIR/X-ray have been used to argue for an expanding plasma model of variable emission in SgrA* (Marrone et al. 2008). At submillimeter wavelengths this mechanism predicts larger sizes for flare structures that might be resolved by VLBI observations, but this model relies on an exact correspondence between individual NIR/X-ray and submillimeter flares, which remains uncertain (Meyer et al. 2008). Regardless of the source of variability at millimeter wavelengths, VLBI has the potential to confirm conclusively its association with the inner disk of Sgr A*, to probe the size of the region of variability (since an interferometer acts as a spatial filter on the emission), and to extract any intrinsic structural periodicity.

Preliminary studies involving the analysis of simulated data from expected models are important for a number of reasons. Such studies will highlight the abilities and limitations of millimeter VLBI in regards to detecting the signatures of the physical processes in the accretion disk surrounding the black hole in Sgr A*. Critical resources (such as stable frequency standards, high-bandwidth recording equipment, and phased-array processors) are likely to be limited initially, and telescope upgrades (such as surface accuracy improvement, expanded IF bandwidth, additional receiver bands, and simultaneous dual-polarization capability) must necessarily be prioritized. Simulated observational data can help assess the tradeoffs that must be considered for optimization of Galactic Center VLBI observations. The ultimate goal is to explore the potential of black hole parameter estimation by present and future millimeter VLBI observations.

In this paper, we explore the observational signatures of an orbiting hot spot embedded in a quiescent disk around Sgr A*. We consider a nonimaging approach to analyzing millimeter VLBI data for several reasons. First, one fundamental assumption of Earth rotation aperture synthesis is that the source structure is not changing. Since orbital periods in the hot spot models are much shorter than the rotation of the Earth, this assumption is clearly violated. Second, phase-referencing the data is presently not feasible at millimeter wavelengths since the phase path through the atmosphere changes on a timescale which is faster than the time needed to move the antennas between the reference source and Sgr A*. We note, though, that this problem could be circumvented at connected-element arrays where some antennas could be dedicated to simultaneously observing a reference source while others observe Sgr A*, but this is also currently limited by the low signal-to-noise ratio (S/N) that can be achieved in the coherence time of the atmosphere. Potential arrays for millimeter VLBI will have a small number of telescopes, initially as few as three, possibly with vastly different sensitivities. Low expected S/N on some baselines combined with the few antennas available will prevent adequate self-calibration via closure relations. Third, even if the visibility data could be properly calibrated and the source structure were not changing over the observation, the (u, v) plane would be sparsely populated with noisy data points, resulting in poor image fidelity, as shown by the simulations of Miyoshi et al. (2004). At least initially, it will be more productive to analyze the data by model fitting in the visibility domain rather than in the image domain.

2. MODELS OF SGR A*

Models for the flaring emission of Sgr A* at millimeter wavelengths necessarily require a number of components. These are conveniently decomposed into models for the quiescent emission and models for the short-timescale dynamical phenomena responsible for the flare. Any such model has a number of existing observational constraints that it must meet, including reproducing the observed spectra & polarization properties of the quiescent & flaring emission and the dynamical properties of the flare light curves. Here, we describe a set of flare models involving orbiting hot spots embedded within a large-scale accretion flow that are consistent with all existing observations, based upon those described in Broderick & Loeb (2006b).

2.1. Quiescent Emission

Sgr A* is only beginning to become optically thin at millimeter wavelengths. Due to relativistic effects this does not happen isotropically (e.g., Broderick & Loeb 2006a). Therefore, the opacity of the underlying accretion flow is important for both imaging the black hole's silhouette and for the variability arising from hot spots on compact orbits.

Despite being faint compared to the Eddington luminosity for a $4 \times 10^6\,M_\odot$ black hole, Sgr A* is still considerably bright, emitting a bolometric luminosity of approximately $10^{36}\,\mathrm{erg\,s^{-1}}$. For this reason, it has been widely accepted that Sgr A* must be accretion powered, implying a minimum accretion rate of at least $10^{-10}\,M_\odot\,\mathrm{yr}^{-1}$. It is presently unclear how this emission is produced. This is evidenced by the variety of models that have been proposed to explain the emission characteristics of Sgr A* (e.g., Narayan et al. 1998; Blandford & Begelman 1999; Falcke & Markoff 2000; Yuan et al. 2002, 2003; Loeb & Waxman 2007). Models in which the emission arises directly from the accreting material have been subsumed into the general class of Radiatively Inefficient Accretion Flows (RIAF), defined by the weak coupling between the electrons, which radiate rapidly, and the ions, which efficiently convert gravitational potential energy into heat (Narayan et al. 1998). This coupling may be sufficiently weak to allow accretion flows substantially in excess of the $10^{-10}\,M_\odot\,\mathrm{yr}^{-1}$ required to explain the observed luminosity with a canonical radiative efficiency.

Nevertheless, following the detection of polarization from Sgr A* above 100 GHz (Aitken et al. 2000; Bower et al. 2001, 2003; Marrone et al. 2006), and subsequent measurements of the Faraday rotation measure (Macquart et al. 2006; Marrone et al. 2007), the accretion rate near the black hole has been inferred to be significantly less than the Bondi rate, implying the existence large-scale outflows (Agol 2000; Quataert & Gruzinov 2000). Therefore, in the absence of an unambiguous theory, we adopt a simple, self-similar model for the underlying accretion flow which includes substantial mass loss.

Following Yuan et al. (2003), this model is characterized by a Keplerian velocity distribution, a population of thermal electrons with density and temperature

$$n_{e,\rm th} = n^0_{e,\rm th}\left(\frac{r}{R_{\rm S}}\right)^{-1.1} e^{-z^2/2\rho^2} \quad \text{and} \quad T_e = T^0_e\left(\frac{r}{R_{\rm S}}\right)^{-0.84}, \tag{1}$$

respectively, a population of nonthermal electrons

$$n_{e,\rm nth} = n^0_{e,\rm nth}\left(\frac{r}{R_{\rm S}}\right)^{-2.9} e^{-z^2/2\rho^2}, \tag{2}$$

and spectral index $\alpha_{\rm disk} = 1.25$ (defined as $S \propto \nu^{-\alpha_{\rm disk}}$), and a toroidal magnetic field in approximate ($\beta = 10$) equipartition with the ions (which produce the majority of the pressure), i.e.,

$$\frac{B^2}{8\pi} = \beta^{-1} n_{e,\rm th}\frac{m_p c^2 R_{\rm S}}{12r}. \tag{3}$$

In all of these equations, the radial structure was taken directly from Yuan et al. (2003), and the vertical structure was determined by assuming that the disk height is comparable to the polar radius, ρ. Since the accreting plasma is becoming optically thin at millimeter wavelengths, both special and general relativistic effects are essential to Sgr A*'s millimeter and submillimeter spectrum. These were, however, neglected in favor of tractability in Yuan et al. (2003). Here, we correct for this by determining $n^0_{e,\rm th}$, T^0_e & $n^0_{e,\rm nth}$ via a fit of Sgr A*'s observed radio, submillimeter and near-infrared spectrum with that produced by our model RIAF, computed using a fully relativistic ray-tracing code (described in more detail below and in Section 2.3). For every inclination and black hole spin presented here this was possible with extraordinary accuracy (reduced $\chi^2 < 1$ in all cases and $\lesssim 0.2$ for many), implying that this model is presently significantly under-constrained by the quiescent spectrum alone. It is also capable of producing the Faraday rotation measures observed, and thus the polarimetric properties of Sgr A*.

The primary emission mechanism is synchrotron, arising from both the thermal and nonthermal electrons. We model the emission from the thermal electrons using the emissivity described in Yuan et al. (2003), appropriately altered to account for relativistic effects (see, e.g., Broderick & Blandford 2004). Since we perform polarized radiative transfer via the entire complement of Stokes parameters, we employ the polarization fraction for thermal synchrotron as derived in Petrosian & McTiernan (1983). In doing so we have implicitly assumed that the emission due to thermal electrons is isotropic, which while generally not the case is unlikely to change our results significantly. For the nonthermal electrons we follow Jones & O'Dell (1977) for a power-law electron distribution, cutting the electron distribution off below a Lorentz factor of 10^2 and corresponding to a spectral index of $\alpha_{\rm disk} = 1.25$, both roughly in agreement with the assumptions in Yuan et al. (2003). For both the thermal and nonthermal electrons the absorption coefficients are determined directly via Kirchoff's law.

2.2. Flares

The rapid NIR and X-ray variability of Sgr A* exhibits substructure on minute timescales, implying that the source of variable emission in these bands is localized to sub-horizon scales. Presently, though, the size scales of submillimeter flares are unclear. Recent multi-wavelength campaigns have suggested that submillimeter flares lag behind their NIR counterparts in some cases (Marrone et al. 2008), which has been interpreted in terms of an adiabatically expanding emission region at longer wavelengths that would be much larger than the size ($< 4R_{\rm S}$) found for the submillimeter quiescent emission (Doeleman et al. 2008). However, submillimeter wavelength flares also exhibit substructure in flux density, polarization fraction, and polarization angle (Marrone et al. 2006) on timescales similar to variations observed in the NIR and X-ray. These short-term variations would seem to indicate that, in fact, there is substantial flare structure on scales of a few $R_{\rm S}$ in the submillimeter.

Claims of periodicity in some NIR flares (Genzel et al. 2003; Bélanger et al. 2006) suggest that at least a subset of these flares could arise from orbiting hot spots (Broderick & Loeb 2005; Melia et al. 2001). In a recent analysis of a 600 minute NIR light curve, Meyer et al. (2008) suggest that the picture is more complex. Nevertheless, hot spot features are a natural consequence of the dissipation required in black hole accretion flows. Strong magnetic turbulence, driven, e.g., by the magnetorotational instability, will unavoidably produce nonthermal electrons at strong shocks and magnetic reconnection events. Generally, the production of these nonthermal electrons will be most prominent in the innermost regions of the accretion flow, where the magnetic turbulence is strongest. Thus, in this paper we adopt an orbiting hot spot model for the flaring activity in SgrA*, noting that such emission should be more easily observed in the submillimeter. In the NIR, the synchrotron cooling time is comparable to a single orbit, and thus periodicity would appear only when energetic electrons are produced over an extended period (see Equation (4)). In contrast, at millimeter wavelengths, the synchrotron cooling time is many hours, and thus multiple orbits of a single hot spot would be observable.

Therefore, for concreteness, we model the flare emission by a localized, orbiting overdensity in the nonthermal electron distribution. It is important to note that the region producing the flare need not be dynamically important. Within the context of a RIAF model for the accretion flow onto Sgr A*, the pressure is overwhelmingly dominated by the ions. This is a direct consequence of the assumed weak coupling between the electrons and ions, and thus the low luminosity of the accretion flow. For typical RIAF accretion rates ($10^{-8}\,M_\odot\,{\rm yr}^{-1}$), the luminosity would need to be increased by orders of magnitude before the nonthermal electrons become dynamically significant. For the observed flares, which typically do not increase the NIR luminosities by more than a single order of magnitude, this means that the accelerated electrons will be frozen into the accretion flow. In this case, the size of the emitting region, $2\Delta r$, is determined by the scale of the magnetic turbulence.

The dominant constraints upon the lifetimes of hot spots in the accretion flow are Keplerian shear and synchrotron cooling. Hot spots will shear apart on roughly $r/\Delta r$ orbital periods, and thus small spots will last many orbits. Unlike shear, cooling is not achromatic, with the flare cooling more rapidly at higher frequencies. The cooling time is approximately

$$\tau_{\rm c} \simeq 3\left(\frac{\lambda}{1\,{\rm mm}}\right)^{1/2}\left(\frac{B}{30\,{\rm G}}\right)^{-3/2}{\rm hr}, \tag{4}$$

which should be compared to the period at the ISCO, ranging from 30 minute for a nonrotating black hole to 4 minute for a maximally rotating black hole. Thus, we expect that hot spots will typically survive many orbits at millimeter and submillimeter wavelengths.

Our hot spot model consists of a locally spherically symmetric, Gaussian overdensity of nonthermal electron. Explicitly, given $\Delta x^\mu = x^\mu - x^\mu_{\rm spot}$ and a scale, $R_{\rm spot} = 0.75 R_{\rm S}$, the hot spot density is

$$n_{e,\rm spot} = n^0_{e,\rm spot} \exp\left[-\frac{\Delta x^\mu \Delta x_\mu + \left(u^\mu_{\rm spot} \Delta x_\mu\right)^2}{2R^2_{\rm spot}} \right], \quad (5)$$

where the hot spot 4-velocity $u^\mu_{\rm spot}$ is assumed to be the same as that of the underlying disk (which we have chosen to be Keplerian). Our description of the hot spot is completed by the spectral index of the power-law distribution of electrons, $\alpha_{\rm spot} = 1.3$, taken from observations of NIR flares (Eckart et al. 2004). Like the disk, the hot spot radiates primarily via synchrotron.

2.3. Generating Images

The method by which images of the flaring disk are produced is discussed at length in Broderick & Blandford (2003; see also Broderick & Loeb 2006a, 2006b). As a result, we only briefly summarize the procedure here.

Null geodesics are constructed by integrating a Hamiltonian formulation of the geodesic equations

$$\frac{dx^\mu}{d\eta} = f(x^\sigma) k^\mu \quad \text{and} \quad \frac{dk_\mu}{d\eta} = -\frac{f(x^\sigma)}{2} \frac{\partial k^\nu k_\nu}{\partial x^\mu}\bigg|_{k_\alpha}, \quad (6)$$

where $f(x^\sigma)$ is an arbitrary function, corresponding to the freedom inherent in the affine parameterization, η. In order to regularize the affine parameterization near the horizon, we choose

$$f(x^\sigma) = r^2 \sqrt{1 - \frac{r}{r_{\rm h}}}, \quad \text{where} \quad r_{\rm h} = \frac{R_{\rm S}}{2}\left(1 + \sqrt{1 - a^2}\right) \quad (7)$$

is the horizon radius (a is the dimensionless black hole spin). It can be explicitly shown that this does reproduce the null geodesics (Broderick & Blandford 2003).

The relativistic generalization of the radiative transfer problem is most easily obtained by directly integrating the Boltzmann equation (Lindquist 1966; Broderick & Loeb 2006a). In this case, it is the photon distribution function, $N_\nu \propto I_\nu/\nu^3$ (which has the virtue of being a Lorentz scalar), that is evolved. In the case of polarized transfer, it is possible to define the covariant analogues of the Stokes parameters, $\mathbf{N}_\nu = \left(N_\nu, N^Q_\nu, N^U_\nu, N^V_\nu\right)$, in terms of a parallel propagated tetrad (Broderick & Blandford 2004). In terms of these, the radiative transfer equation takes on its standard form

$$\frac{d\mathbf{N}_\nu}{d\eta} = \bar{\mathbf{j}}_\nu - \bar{\boldsymbol{\alpha}}_\nu \mathbf{N}_\nu, \quad (8)$$

where $\bar{\mathbf{j}}$ and $\bar{\boldsymbol{\alpha}}_\nu$ are the appropriately generalized emission and absorption coefficients, and may be trivially related to the same quantities in the local plasma frame (Lindquist 1966; Broderick & Blandford 2004; Broderick 2006).

Images are produced by tracing a collection of initially parallel null geodesics from pixels on a distant plane backwards in time, toward our model of Sgr A*, terminating the ray when it has been captured by the black hole, escaped the system, or accrued an optical depth greater than 10. Along each ray we integrate the polarized radiative transfer, obtaining $\mathbf{N}_\nu$ at the original plane. We construct 100 such images with resolutions of 128×128 pixels for each hot spot orbit. This procedure is repeated for each frequency of interest, for which we keep the underlying physical model fixed. Thus, for each spin/inclination pair, the relationship between 230 GHz and 345 GHz images is dictated by the spectral properties of the source.

3. VLBI ANALYSIS

3.1. Techniques

Typical VLBI analysis techniques employ an iterative "self-calibration" loop, whereby a sky brightness model, the VLBI data, and a series of complex gains for each VLBI site are brought into convergence (Cornwell & Wilkinson 1981). This process relies on the assumption that all array calibration can be expressed as station-based gains, which is equivalent to requiring that all calibration errors "close", or cancel when computed over suitable closed loops of VLBI baselines. In almost all cases, this assumption is valid, and closure quantities can be constructed from the data, which contain structural information on the observed source, but that are largely immune to station-based phase and gain errors (Jennison 1958; Twiss et al. 1960). However, closure quantities alone are insufficient to determine baseline phases for a VLBI array. The number of independent closure phases computed over closed triangles of VLBI stations, for example, grows as $\frac{1}{2}(N-1)(N-2)$, where N is the number of antennas, while the number baseline phases in the array will be $\frac{1}{2} N (N-1)$. The fraction of visibility phase information available from closure phases is thus $(N-2)/N$. For millimeter VLBI, N will be small (initially $N = 3$ or 4; Section 3.2), and closure quantities will not be sufficiently numerous to allow for full calibration of the data. However, closure quantities are robust observables and can therefore be used for model fitting even when baseline-based visibilities are contaminated with station-based phase and gain errors. Indeed, closure quantities have been successfully used for model fitting (e.g., Rogers et al. 1974), including recent experiments to place limits on the apparent size and structure of Sgr A* at wavelengths as short as 3 mm (Doeleman et al. 2001; Bower et al. 2004; Shen et al. 2005; Markoff et al. 2007).

Closure phase and amplitude in the weak-detection limit are discussed in detail by Rogers et al. (1995). We summarize the most relevant information below.

The closure phase is the sum of the baseline phases along a triangle of antennas. It is independent of instrumental and atmospheric complex gain terms. The closure phase of a symmetric distribution of emission is always zero or 180° (e.g., Monnier 2007). Deviations from these values are indicative of asymmetries (about the origin) in the source structure on the size scales probed by the baselines of the triangle. A static asymmetric source structure will show slow variations in closure phase over the course of observations due to the rotation of the Earth, which changes the projected length and orientation of baselines. If the source structure is changing, as would be the case for an orbiting hot spot, the closure phase on some triangles will change as well. Because the timescale of hot spot orbits near the black hole is on the order of tens of minutes (depending on the mass and spin of the black hole and the orbital radius of the hot spot), closure phase variability will be much more rapid for the case of a hot spot embedded in a disk as compared to a quiescent disk alone. Since a hot spot may survive for several orbits before cooling or shearing (Section 2), closure phases can exhibit approximate periodic behavior over several cycles. Thus,

Table 1
Assumed Telescope Parameters

Facility	N[a]	Diameter[a] (m)	230 GHz?	SEFD[b] (Jy)	345 GHz?	SEFD[b] (Jy)
Hawaii	8	23	Yes	4900	Yes	8100
CARMA	8	27	Yes	3500	Planned	4900
SMT	1	10	Yes	11,900	Yes	23,100
LMT	1	32	Planned	10,000[c]	No	13,700[d]
ASTE	1	10	No	...	Yes	14,000
APEX	1	12	Soon	6500	Yes	12,200
ALMA	10	38	Soon	500	Soon	1000
PV	1	30	Yes	2900	No	5200[d]
PdB	6	37	Yes	1600	Soon	3400

Notes.
[a] Effective aperture when number of antennas (N) are phased together.
[b] Expected system equivalent flux density values at 230 and 345 GHz toward Sgr A* include typical weather conditions and opacities.
[c] Completion of the dish and upgrades to the surface accuracy and receiver will eventually lower the SEFD by more than a factor of 10.
[d] These telescopes do not presently have planned 345 GHz capability. Assumed SEFD values are for illustrative purposes only.

closure phases are appropriate observables for detecting periodic source structure changes on short timescales. The S/N of the closure phase is dominated by the lowest S/N of the visibility data along the three segments.

The closure amplitude is constructed as the ratio of products of visibility amplitudes (A) along a quadrangle of antennas. For four antennas a, b, c, and d, two independent closure amplitudes can be constructed:

$$A_{abcd} \equiv \frac{|A_{ab}||A_{cd}|}{|A_{ac}||A_{bd}|} \quad \text{and} \quad A_{adbc} \equiv \frac{|A_{ad}||A_{bc}|}{|A_{ac}||A_{bd}|}. \qquad (9)$$

For an array of N antennas, there are $\frac{1}{2}N(N-3)$ independent closure amplitudes. As for closure phase, the closure amplitude is unaffected by gain calibration errors on each of the antennas. Deviations of the closure amplitude from unity are usually indicative of resolved, asymmetric source structure. Large excursions in closure phase and amplitude are often correlated, since small changes with time in the complex visibility, due to Earth rotation or source structure changes, have the largest effects on the phase when the visibility amplitude is near zero. Since a small visibility amplitude results in a very small closure amplitude if it appears in the numerator, and a very large closure amplitude if it appears in the denominator, closure amplitudes are generally presented on logarithmic scales.

In the low-signal regime, the closure amplitude is a biased quantity. The detected visibility amplitude on a baseline is the modulus of the vector (amplitude and phase) sum of the signal and the noise and is by definition nonnegative. When the S/N is small, the visibility amplitude is dominated by the noise amplitude and is therefore larger than the signal amplitude. Thus, if the source is not detected on baseline ab but is detected on baselines cd, ac, and bd, the closure amplitude A_{abcd} will on average be larger than the value predicted by a noiseless model of the source structure. The closure phase does not suffer from a similar bias.

3.2. Antennas

Whereas centimeter wavelength astronomy can be performed from virtually any location with a clean spectrum, potential sites for (sub)millimeter wavelength astronomy are limited by the need to be above most of the water vapor content in the atmosphere. Consequently, possible arrays for millimeter VLBI are sparser than for centimeter VLBI. In this section, we summarize the best prospects for millimeter VLBI among existing telescopes and those that may come on line in the near future.

Hawaii. The Caltech Submillimeter Observatory (CSO), James Clerk Maxwell Telescope (JCMT), and Submillimeter Array (SMA) are all located atop Mauna Kea. Each telescope can observe in both the 230 and 345 GHz bands. The JCMT has a single-polarization 230 GHz receiver and a dual-polarization 345 GHz receiver. The SMA presently does not support simultaneous dual-polarization observations but is expected to do so eventually at 345 GHz. Development of instrumentation to phase together the CSO, JCMT and several SMA dishes is underway, and will result in an effective 23 m aperture, which we refer to as "Hawaii," by early 2009.

CARMA. The Combined Array for Research in Millimeter-wave Astronomy (MWA) consists of six 10.4 m antennas and nine 6.1 m antennas. The ability to phase together up to eight CARMA dishes for VLBI is planned, and will result in an effective 27 m aperture. CARMA can presently observe in the 230 GHz band. A future upgrade to include 345 GHz is planned, but it is unclear when this band will be available for observations. We also consider a single 10.4 m dish at 230 GHz ("CARMA-1") in Section 4.3.

SMTO. The Arizona Radio Observatory Submillimeter Telescope (SMT) on Mt. Graham in Arizona is a 10 m dish capable of observing at both 230 and 345 GHz.

LMT. The Large Millimeter Telescope (LMT), presently under construction, will be a 50 m dish capable of observing at both the 230 and 345 GHz bands. When complete, it will be the most sensitive millimeter telescope in the Northern hemisphere. In anticipation that the LMT collecting area will be installed in phases, we conservatively adopt an effective aperture of 32 m.

Chile. Several millimeter telescopes are available in Chile. The Atacama Submillimeter Telescope Experiment (ASTE) is a 10 m dish with a single-polarization receiver at 345 GHz. The Atacama Pathfinder Experiment (APEX) is a 12 m dish with a double sideband (DSB) at 345 GHz. Future two sideband (2SB) heterodyne receivers capable of observing at 230 GHz and 345 GHz are under construction. We refer to using one of these facilities as "Chile-1." ALMA will be composed of a large number of 12 m dishes with 2SB receivers at both 230 and 345 GHz. We also consider the possibility of a 10-element phased ALMA station as the Chilean site ("Chile-10"), since our models do not produce much expected signal on the long baselines to Chile (Section 3.3).

Pico Veleta. The 30 m Institut de Radioastronomie Millimétrique (IRAM) telescope on Pico Veleta (PV) can observe at 230 GHz.

Plateau de Bure. The IRAM PdB Interferometer consists of six 15 m telescopes equipped with 230 GHz receivers. An upgrade to add 345 GHz capability is presently under construction and is expected to be available in late 2008. The six telescopes can currently be phased up over a 256 MHz bandwidth into a single 37 m equivalent aperture. Extension to higher bandwidths will require instrumentation development similar to what will be deployed to phase up the antennas on Mauna Kea.

A summary of telescope capabilities is given in Table 1. Sensitivity is given in terms of the system equivalent flux density (SEFD), which is equal to $2kT_{\rm sys}/A_{\rm eff}$, where k is Boltzmann's

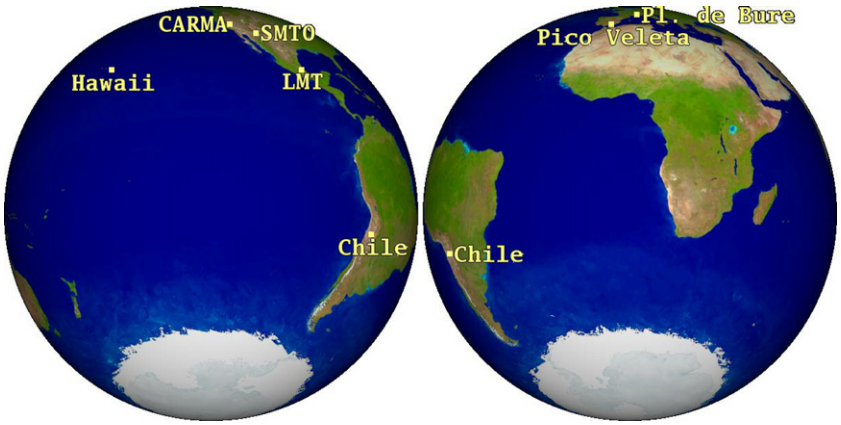

Figure 1. Locations of candidate telescopes for millimeter wavelength VLBI as viewed from the declination of Sgr A*.

constant and the effective area $A_{\rm eff}$ is the product of the geometric area and the aperture efficiency. Assumed $T_{\rm sys}$ values toward Sgr A* include a typical expected atmospheric contribution, which can be quite large for Northern hemisphere telescopes due to the low elevation of the Galactic Center. Since the atmospheric contribution is highly weather-dependent, actual observations may achieve significantly different values of the SEFD at each telescope. SEFD values include a 10% phasing loss factor for phased arrays. All facilities can in principle provide an IF bandwidth of at least 4 GHz, although accessing the full bandwidth at some stations may be problematic. Thus, 32 Gbit s^{-1}, corresponding to 2-bit Nyquist samples of a 4 GHz bandwidth in two orthogonal polarizations, is the maximum possible recording rate that we will consider. At present 16 Gbit s^{-1} digital back ends are still in the planning stage, so initial observations will likely employ a smaller bandwidth. Except as noted, all telescopes can observe two polarizations simultaneously.

The European telescopes (PV and PdB) and the North American telescopes (Hawaii, CARMA, SMTO, and LMT) have no mutual visibility of Sgr A*, except for approximately 1 hr of overlap above 10° elevation on the PV–LMT baseline. Thus, there are only three possible types of subarrays with at least three elements possible among these millimeter facilities: North America only, North America plus Chile, and Europe plus Chile (Figure 1). For our simulations, we take our 230 GHz array to consist of Hawaii, CARMA, SMTO, LMT (32 m), either APEX or a 10-element phased ALMA, PV, and PdB. Early science at 345 GHz will likely consist of the single triangle of Hawaii, SMTO, and a Chilean telescope. However, we consider the same set of telescopes as at 230 GHz in order to illustrate what future 345 GHz upgrades might accomplish.

3.3. Methods

Simulated data were obtained using task UVCON in the Astronomical Image Processing System (AIPS). Synthetic data were produced using an averaging interval of 10 s. Typical coherence times at 230 GHz are 10 s, but can be as low as 2–4 s and, under good weather conditions, as long as 20 s (Doeleman et al. 2002). At the ALMA site in Chile, the measured coherence time of the atmosphere is $>$ 10 s 60% of the time at 230 GHz and 45% of the time at 345GHz (Holdaway 1997). Since AIPS cannot directly handle time-varying source structure, for a hot spot model we simulate data from 100 static, equally spaced time slices in a single hot spot orbit and construct a data set. All data assume 2-bit sampling at the Nyquist rate. Thus, the recording rate (in Gbit s^{-1}) is four times the observing bandwidth (in GHz). For continuum observations at a constant sampling rate, 2-bit quantization achieves sensitivity levels very nearly approaching that of 1-bit quantization at half the observing bandwidth (Thompson et al. 2001), which is limited by the hardware at certain telescopes (Section 3.2).

Observations of total intensity (i.e., Stokes I) theoretically obtain identical noise levels regardless of whether the data are taken at full bandwidth in single-polarization mode or at half bandwidth in dual-polarization mode, provided that circularly polarized feeds are used. The hot spot models do not produce circular polarization (Stokes V) but do produce large amounts of linear polarization (Stokes Q and U), especially on small spatial scales. Circularly polarized feeds measures Stokes visibilities $I \pm V$ and therefore are identical for our models. Dual-polarization observations are essential if linearly polarized feeds are used, since the parallel-hand data are sensitive to the Stokes visibilities $I \pm P$, where P is a linear combination of Stokes Q and U (depending on feed orientation). In practice the observer will usually prefer to observe in dual-polarization mode when available even using circular feeds, since cross-hand correlation products provide polarimetric information as well. The polarimetric products are of special interest, since they may show asymmetries not seen in total intensity (e.g., Bromley et al. 2001). However, we focus on total intensity methods and results in this work and defer polarimetric considerations to a future paper.

In the subsequent discussion, we consider a suite of models parameterized by black hole spin ($a = 0$ nonrotating or $a = 0.9$ highly rotating), disk orientation, and hot spot orbital radius (r). For each spin, the radius of the ISCO ($r_{ISCO} = 6\,R_{\rm G}$ for $a = 0$ and $2.32\,R_{\rm G}$ for $a = 0.9$) and one larger radius are chosen; the larger radius for $a = 0.9$ is chosen to have the same period as the $a = 0$, ISCO model. Disk models assume that the spin axes of the black hole and accretion disk are aligned, with the major axis of the projected disk aligned east–west except in Model C, in which the disk and hot spot are aligned north-south instead. Flux densities have been scaled to match connected-element interferometric observations. Contributions from the quiescent disk are assumed to be approximately 3 Jy, depending slightly on the specific model parameters chosen, as listed in Table 2. A single prograde orbiting hot spot contributes a variable flux density component, depending on orbital phase and the specific model, consistent with submillimeter observations (Marrone

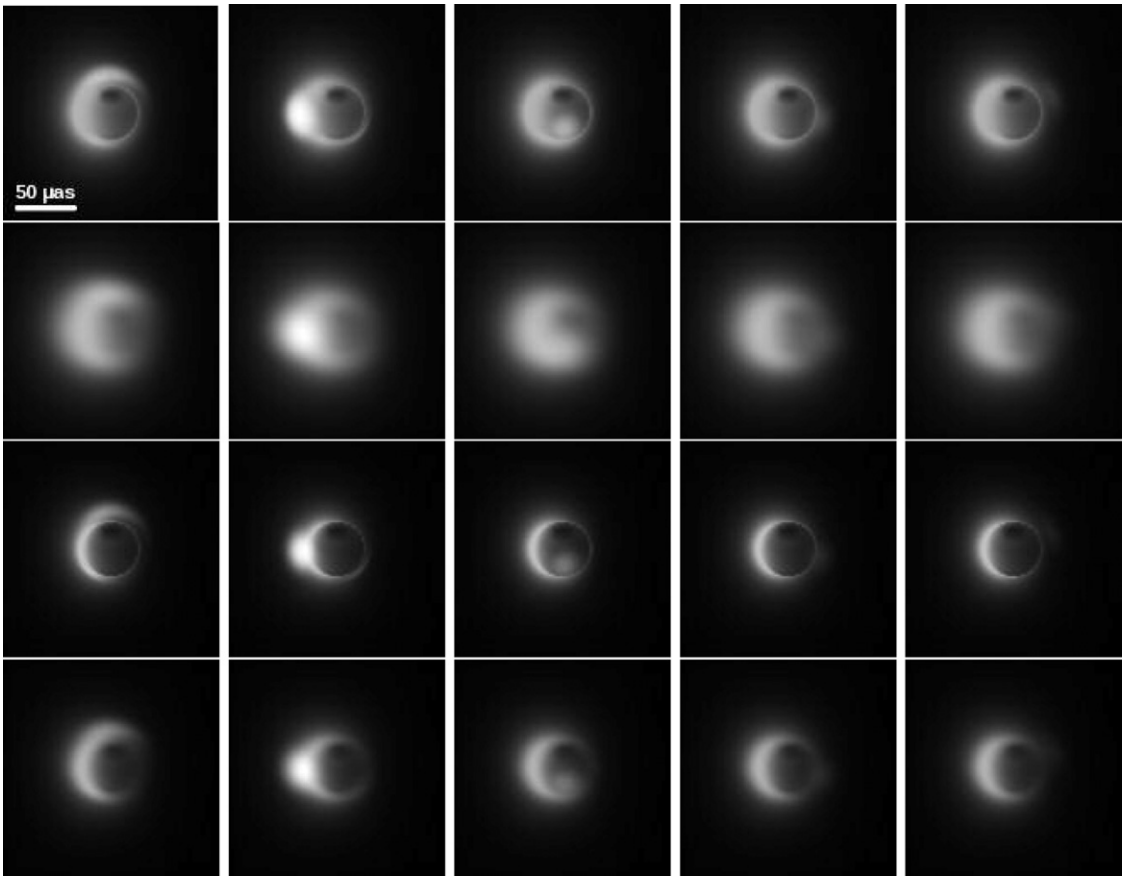

Figure 2. Images of Model B. Columns show orbital phases 0, 0.2, 0.4, 0.6, and 0.8 from left to right. From top to bottom, rows show the input model at 230 GHz, the same model after convolution with expected interstellar scattering at 230 GHz, the model at 345 GHz, and the same model after scattering at 345 GHz.

Table 2
Model Parameters

Model	a (R_G)[a]	Period (minute)	i (°)	P.A.[b] (°)	ν (GHz)	Disk[c] (Jy)	Min[c] (Jy)	Max[c] (Jy)
A	0	27.0	30	90	230	3.19	3.49	4.05
					345	3.36	3.63	5.28
B	0	27.0	60	90	230	3.03	3.05	4.03
					345	2.96	2.99	4.78
C	0	27.0	60	0	230	3.03	3.05	4.03
					345	2.96	2.99	4.78
D	0.9	27.0	60	90	230	2.98	2.99	4.05
					345	2.96	2.97	4.00
E	0.9	8.1	60	90	230	2.98	3.08	4.15
					345	2.96	3.04	6.07
F	0	166.9	60	90	230	3.07	3.08	3.38
					345	2.99	3.00	3.18

Notes.
[a] Spin is given in units of the gravitational radius, $R_G \equiv GMc^{-2} = \frac{1}{2}R_S$.
[b] Disk major axis position angle (east of north).
[c] Flux density of quiescent disk alone and minimum/maximum of system with orbiting hot spot.

et al. 2007). The hot spot contributes some flux density even at the minimum in the light curve, an effect that is most pronounced in the $i = 30°$ models. All models are convolved with the expected interstellar scattering given by (Bower et al. 2006). While these model parameters do not span the entire range of possibilities of the Sgr A* disk system, they do show how changes in model parameters affect the observable quantities. Non-imaging VLBI methods are applicable to all reasonable models for the Sgr A* system. Figure 2 shows a series of images from Model B at both 230 GHz and 345 GHz.

The angular resolution available to potential millimeter VLBI arrays is well matched to potentially interesting scales for observing Sgr A* (Figure 3). The longest baselines, Hawaii–Chile and PdB–Chile, provide fringe spacings of 30–35 μas at 230 GHz and 19–23 μas at 345 GHz, slightly larger than the expected interstellar scattering and only several times R_S. Our models do not produce much detectable signal on these small angular scales (Figure 4), but it is possible that smaller hot spots or disk instabilities (not modeled) will produce greater amplitudes on small angular scales. The shortest baselines, SMTO–CARMA and PV–PdB, provide fringe spacings of 230–1000 μas at 230 GHz and 160–700 μas at 345 GHz.

4. RESULTS

4.1. Closure Phases and Amplitudes

Figure 5 shows predicted closure phases at 230 GHz on selected triangles. The closure phase responses are highly dependent on the physical parameters of the Sgr A* system, but several patterns emerge. Data from the smallest triangles (i.e., those composed of only North American telescopes) achieve a high S/N even at the present maximum recording rate of 4 Gbit s^{-1}. Models with a greater north-south extent (e.g., Models A and C), produce a larger closure phase signature on the small triangles. The S/N on all triangles to Chile-1 is low owing to the small flux on small angular scales. Higher bit rates and the substitution of phased ALMA for Chile-1 greatly increase

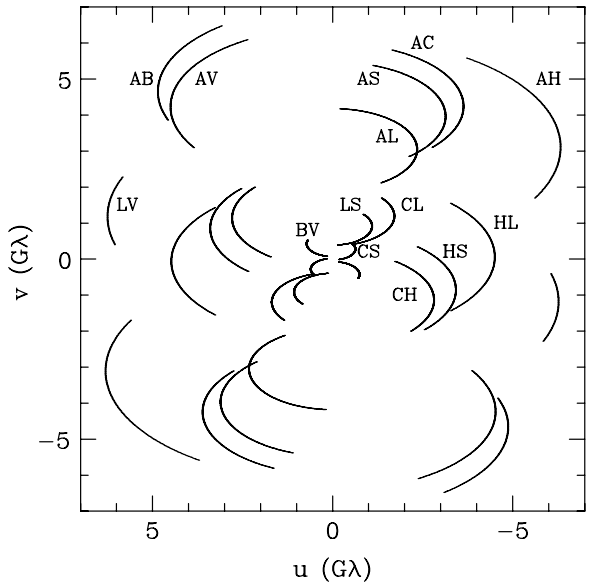

Figure 3. Possible (u, v) tracks for millimeter VLBI. Tracks are labeled by baseline (*A*: ALMA/APEX/ASTE, *B*: Plateau de Bure, *C*: CARMA, *H*: Hawaii, *L*: LMT, *S*: SMTO, *V*: Pico Veleta). Unlabelled tracks correspond to the baseline indicated by $(-u, -v)$. Axes are in units of gigawavelengths at $\nu = 230$ GHz.

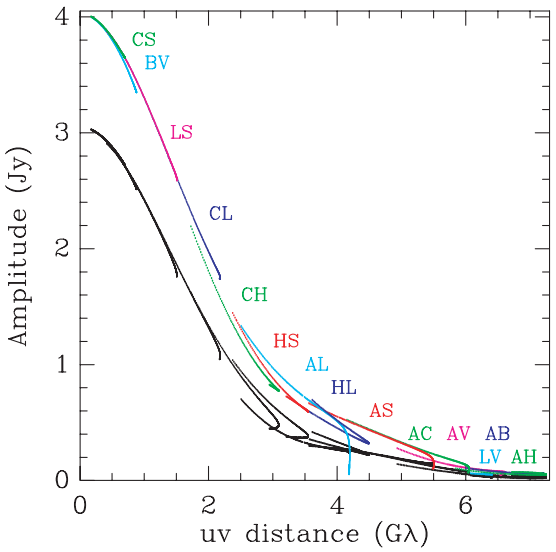

Figure 4. Plot of expected visibility amplitude as a function of baseline length for two frames of Model B230. Symbols show the noiseless visibility amplitudes that would be obtained if the source structure were frozen near minimum (black) and maximum (color) flux in the hot spot orbit. At maximum flux, points are color-coded and labeled by baseline as in Figure 3. Visibility amplitude falls off rapidly with baseline length, and the fractional variability on long baselines can be significantly different than that seen at zero spacing.

detectability, as shown by the third and fourth columns, which correspond to the expected array and recording capabilities in the next few years. Net offsets from zero closure phase on some triangles result from apparent asymmetric structure in the disk caused by lensing and opacity effects.

Figure 6 shows modeled closure phases at 345 GHz. The only available triangle in the near future at 345 GHz will be Hawaii–SMTO–Chile-1, which produces rather low S/N closure phases at 4 Gbit s^{-1}. Of the remaining telescopes, both CARMA and Plateau de Bure plan for 345 GHz receivers in the future. In addition to these, we show triangles including the LMT and Pico Veleta, neither of which has planned 345 GHz capability, to demonstrate what might be seen in the event

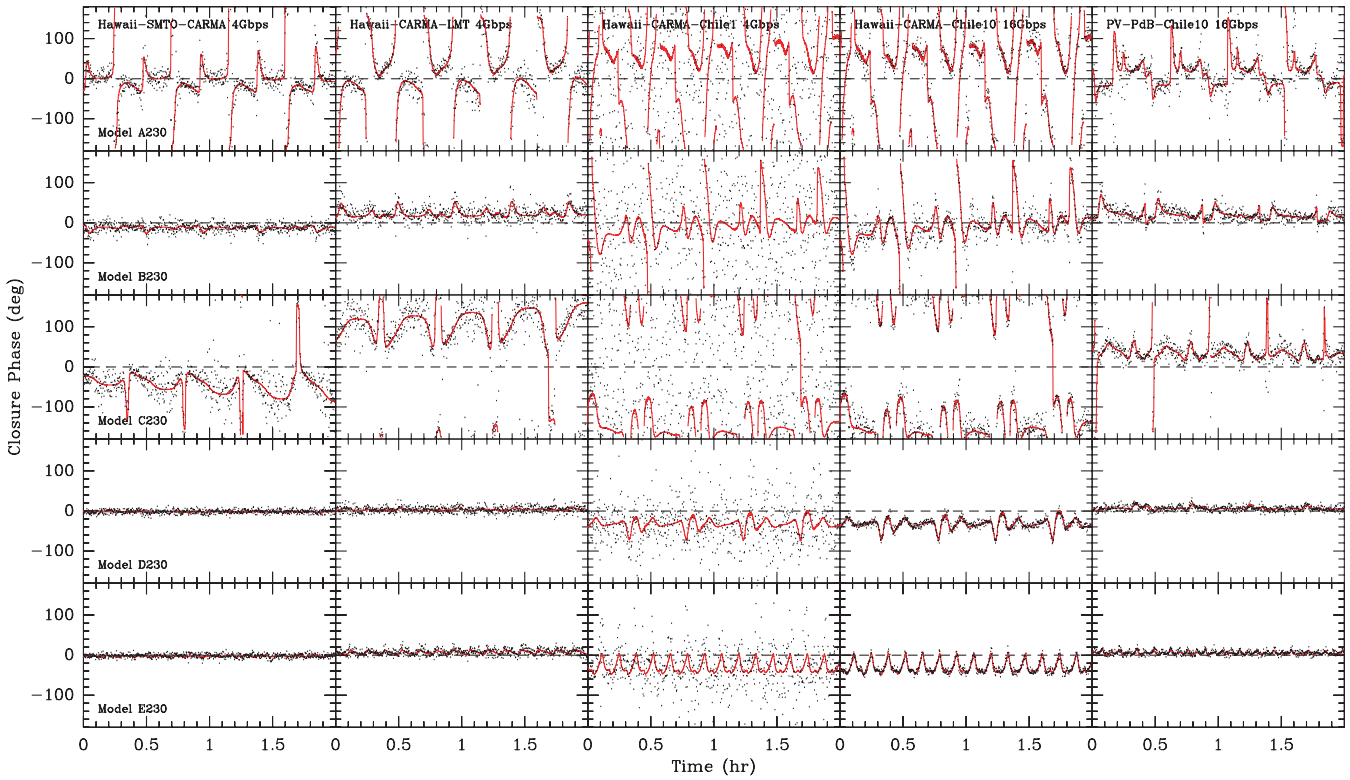

Figure 5. Closure phases on selected triangles at 230 GHz. The solid line (red in the online edition) shows the predicted closure phase in the absence of noise. Each point indicates 10 s of coherently integrated data. The fourth column shows the same triangle as the third column but with a higher data rate and substitution of Chile-10 for Chile-1. The same 2 hr period, corresponding to 4.5 periods (14.8 periods for Model E) is shown in all panels excepting PV-PdB-Chile-10.

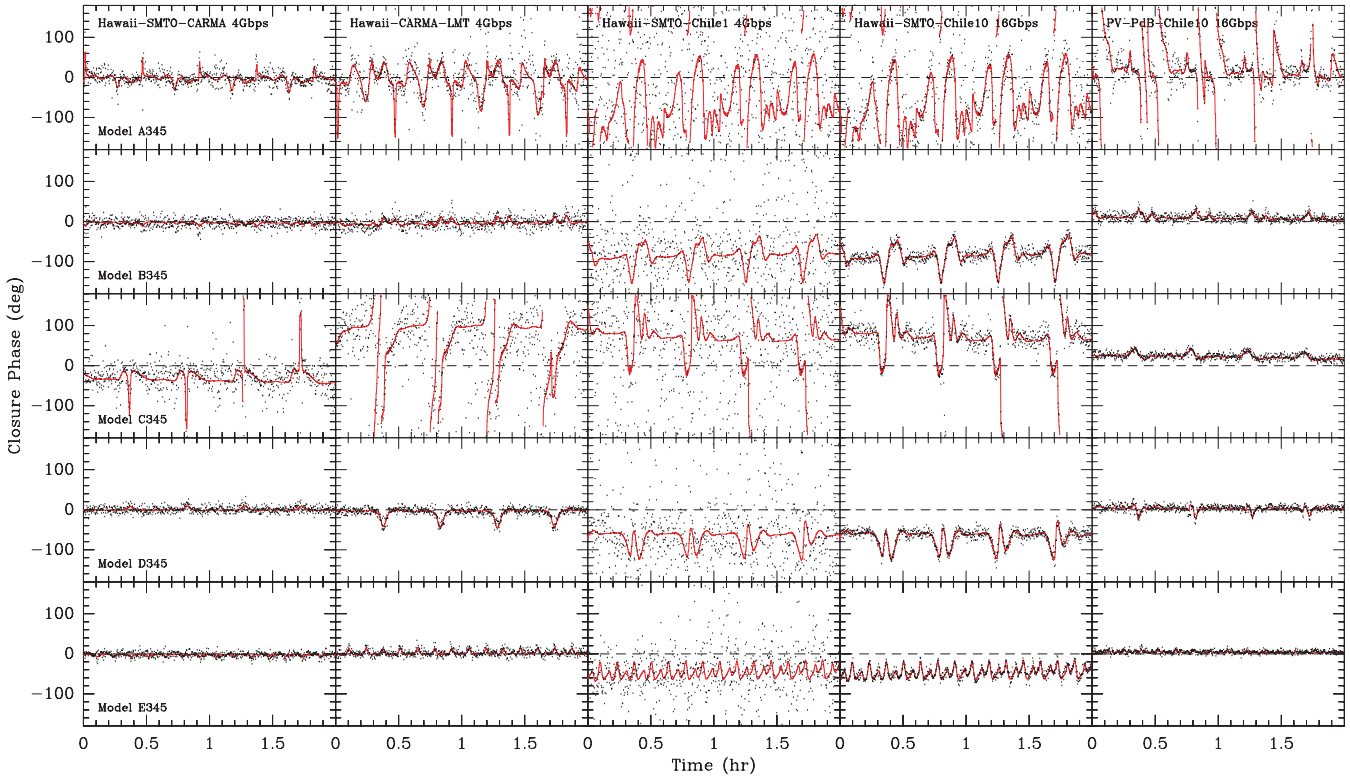

Figure 6. Closure phases on selected triangles at 345 GHz. See Figure 5 for details.
(A color version of this figure is available in the online journal.)

of future upgrades to those facilities. At both 230 GHz and 345 GHz, closure phases on several baseline triangles show clear evidence for periodicity associated with hot spot orbits.

Four telescopes are required to obtain a closure amplitude, which effectively means that closure amplitudes can only be measured on Western hemisphere arrays. Figures 7 and 8 show closure amplitudes on selected quadrangles at 230 and 345 GHz, respectively. Periodicity associated with the orbiting hot spot is evident on most quadrangles. In some models, closure amplitudes including the Hawaii–Chile-1 baseline show bias (as described in Section 3.1) due to the low visibility amplitude on this baseline. The substitution of phased ALMA for Chile-1 combined with higher recording rates suffice to clearly detect Sgr A* on this baseline, resulting in unbiased closure amplitudes. It is possible (and necessary for model fitting) to de-bias closure amplitudes by correcting the visibility amplitudes for the expected noise levels, but the procedure can be difficult when the S/N on a baseline is low (for more details, see Trotter et al. 1998). In any case, the presence of bias does not hinder detection of periodicity.

4.2. Autocorrelation Functions

Signatures of time periodic structure associated with orbiting hot spots can be derived from autocorrelations of closure quantity time series. The autocorrelation function (ACF) of a time series of n closure amplitudes A on a quadrangle of telescopes is given by

$$\mathrm{ACF}_A(k) \equiv \frac{1}{(n-k)\,\sigma^2} \sum_{i=1}^{n-k} [(\log A_i - \mu)\,(\log A_{i+k} - \mu)], \tag{10}$$

where μ and σ^2 are the mean and variance of the distribution of the logarithm of the closure amplitudes, respectively. The logarithm is used in preference to the closure amplitude itself due to the tendency for the closure amplitude to obtain both very small (near 0) and very large values. We also define a variant of the ACF for closure phases, ϕ:

$$\mathrm{ACF}_\phi(k) \equiv \frac{1}{n-k} \sum_{i=1}^{n-k} \cos(\phi_i - \phi_{i+k})\,. \tag{11}$$

This definition has the advantage that it handles phase-wrap ambiguity gracefully, since cos is a periodic function. The normalizations are such that $\mathrm{ACF}(k) = 1$ when k is an integer multiple of the period for a noiseless periodic function. In practice, the peaks of an ACF (other than the trivial peak at $k = 0$, where $\mathrm{ACF}(0) = 1$ by definition) of closure phases or amplitudes fall off with lag rather than returning precisely to unity, because the projected baseline geometries change with Earth rotation. In the case of long periodicities ($\gtrsim$ 2 hr), this effect can be large enough to obscure any periodicity at all on some triangles/quadrangles. While the duration of some SgrA* flare events exceed this time interval, there are claims of modulation within some NIR flares with characteristic timescales of $\sim$ 17 minute (Genzel et al. 2003). From an observational perspective, periodicity is not convincingly detected until at least two full periods (preferably more) have been observed. The longest mutual visibility appears on the SMTO–LMT–Chile triangle, which can see Sgr A* for less than 7 full hours. Triangles including Hawaii or Europe have significantly smaller windows of mutual visibility. The distribution of millimeter telescopes is not optimal for detecting slow periodic variability in Sgr A*.

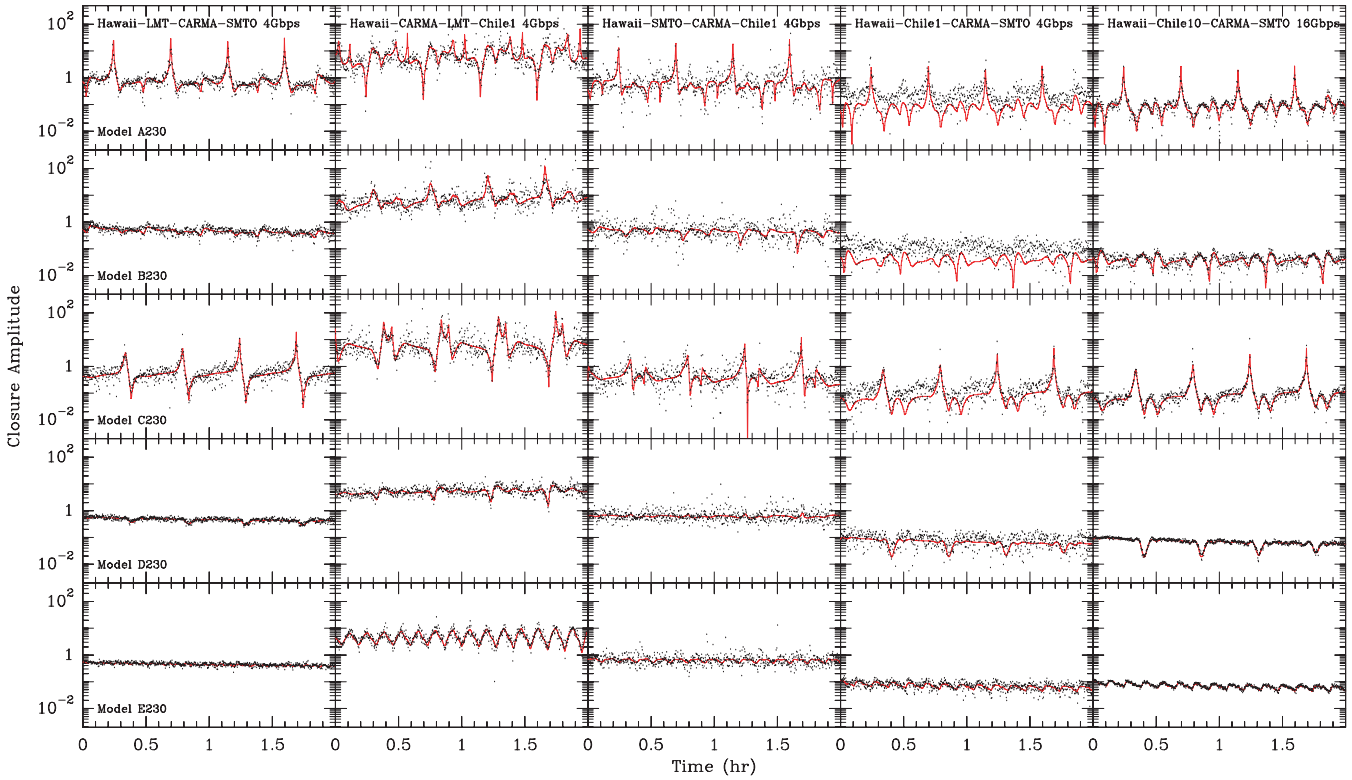

Figure 7. Closure amplitudes on selected quadrangles at 230 GHz. See Figure 5 for details.
(A color version of this figure is available in the online journal.)

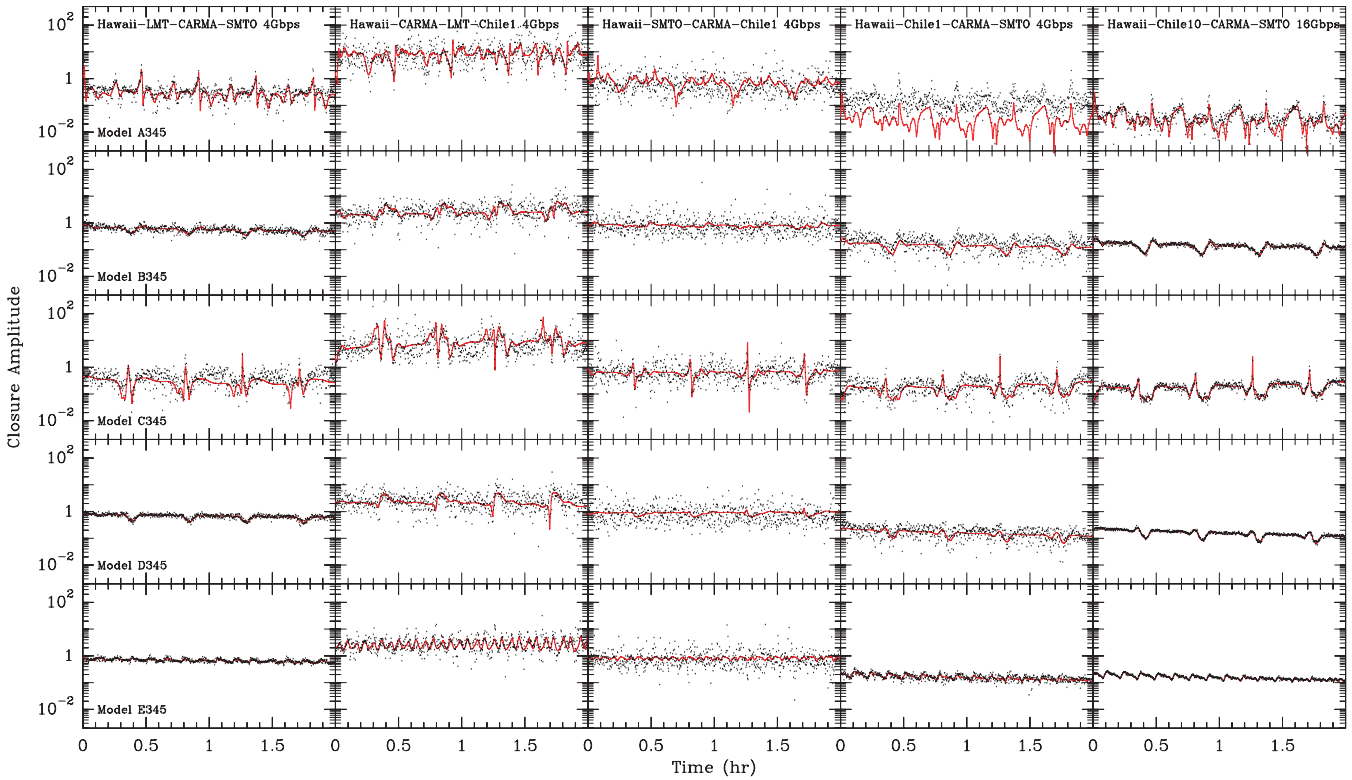

Figure 8. Closure amplitudes on selected quadrangles at 345 GHz. See Figure 5 for details.
(A color version of this figure is available in the online journal.)

The largest nontrivial peak in the ACF indicates the period of the hot spot orbit, as indicated in Figure 9, excluding the slow periodic case. The ACF correctly identifies the period in all models at all recording rates provided that the average S/N $\gtrsim$ 1 and that the triangle contains at least one baseline long enough to be sensitive to the changing source structure. On the

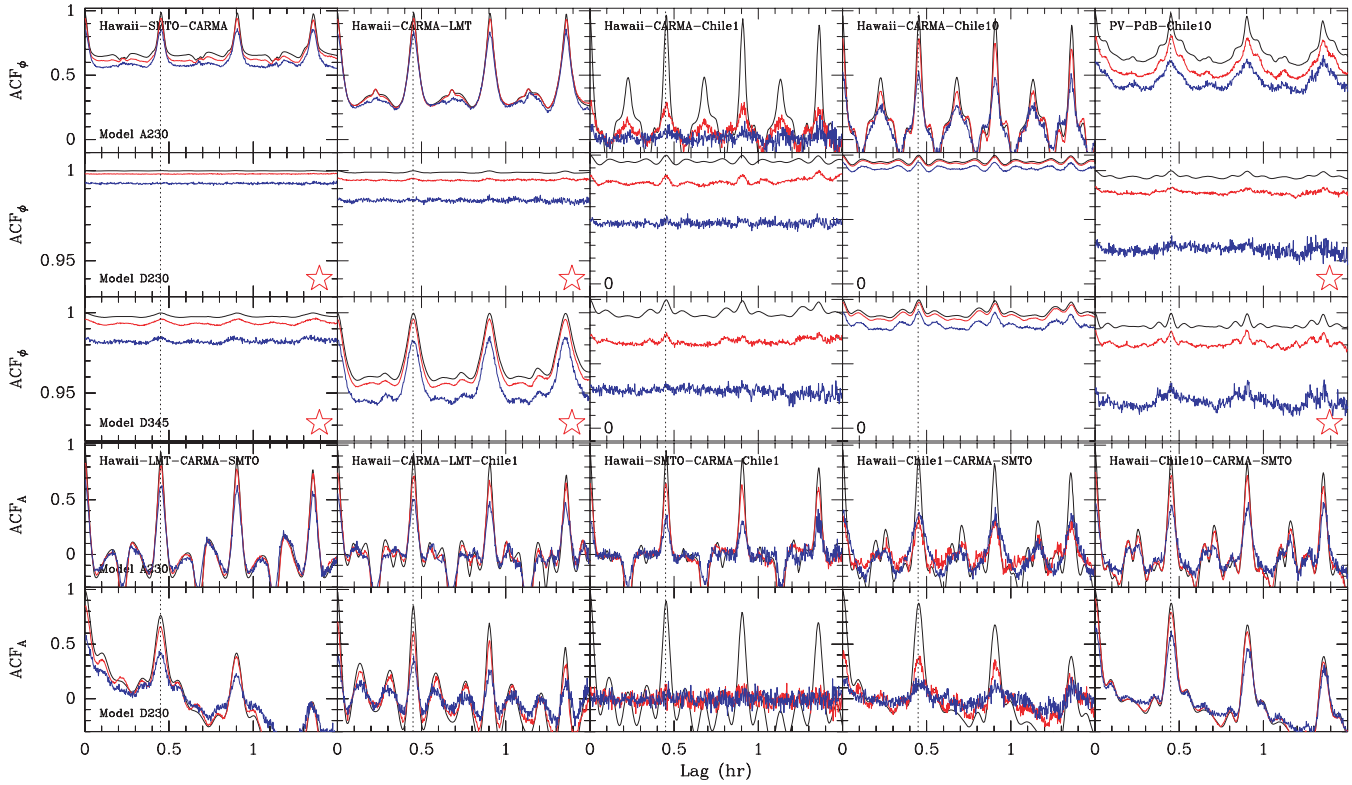

Figure 9. Autocorrelation function plots of selected triangles and quadrangles. Representative models are shown. Black, red, and blue lines indicate ACFs for noiseless data, 16 Gbit s^{-1}, and 4 Gbit s^{-1}, respectively. Panels marked with a red star show ACF$_\phi$ on a different ordinate scale, as indicated to the left in that row; other panels in the same row are on the scale show in the upper left panel. The dotted line shows the period of the hot spot orbit.

small triangles, ACF$_\phi(k)$ shows little variation as a function of lag k, since the phase ACF of a nearly constant function is itself nearly constant. However, small peaks are visible in the ACF on the Hawaii–SMTO–CARMA and Hawaii–CARMA–LMT triangles in Figure 9. The large S/N on the small triangles, due to the fact that the shorter baselines do not resolve out much of the source flux density, permits detectability for reasonable bandwidths.

In addition to the peak at the period, the ACF has peaks at integer multiples of the period. In the weak-detection limit, this may be an important discriminator indicating that the detected period is real. While purely random noise may produce peaks in the ACF, there is no reason why it should produce periodic peaks. At the other end of timescales, intraperiod sub-peaks in the ACF may be produced depending on the details of the source structure and array geometry. Excluding long-period orbits, it is usually clear which peak indicates the orbital period of the hot spot, since the sub-peaks are of smaller amplitude. Nevertheless, it is possible that pathological cases exist in which the observer may misidentify the orbital period. For instance, two identical hot spots at the same radius but separated by 180° in azimuth would produce strong peaks in the ACF at both integer and half-integer multiples of the period, which would lead to a conclusion that the orbital period is half of its true value. A similar ambiguity could arise if the observed variability is produced, for instance, by the rotation of a pattern produced by a two-armed Rossby wave instability (e.g., Falanga et al. 2007).

The key point about the ACF plots is that for the same model, *all triangles and quadrangles indicate the same period*. It will be important to observe with as many telescopes as possible simultaneously, since the extra information provided by the additional telescopes may be important for detecting or confirming marginally detected variability. Three antennas provide a single closure phase, for a total of one ACF; four antennas provide three independent-closure phases and two independent-closure amplitudes, for a total of five independent ACFs; and five antennas provide six closure phases and five closure amplitudes, for a total of 11 independent ACFs. Even if the source is not detected on one long baseline, resulting in a biased closure amplitude, the ACF may still clearly indicate periodicity (e.g., the Hawaii–Chile-1–CARMA–SMTO panel for Model A230 in Figure 9).

4.3. Detecting Periodicity with Likely Arrays

We consider potential observing arrays that may be employed in observations of Sgr A*. The minimum number of telescopes required to produce a closure quantity is 3, and the maximum number of telescopes located at substantially different sites with mutual visibility of Sgr A* is 5. At 230 GHz, we consider western hemisphere arrays consisting of the US triangle; US and Chile-1; US, Chile-1, and the LMT; and the same array with Chile-10 instead. We also consider European–Chile arrays. Since PV is not expected to have 345 GHz capability in the near future, we expect that Chile-10 will exist before 345 GHz observations are possible on the Europe–Chile triangle. Likewise, we expect that western hemisphere arrays will include Chile-10 before the LMT is available at 345 GHz, since 345 GHz capability is not currently planned at the LMT.

For each array, we generate ACF$_\phi$ for each triangle of three antennas and ACF$_A$ for each quadrangle of four antennas. The ACFs can be combined to produce a single combined ACF of the entire array. For optimum detectability, it is necessary to weight the individual ACFs by the square of their effective S/N$_{\rm ACF} \equiv X/\xi$, where X and ξ quantify the effective signal and

noise in the ACF, respectively. For definiteness, we take ξ as the rms deviation in the ACF after a five-channel boxcar-smoothed S/N has been subtracted. We define $X \equiv \max(\mathrm{ACF}(k)) - \max(minute(\mathrm{ACF}(k)), 0), k \neq 0$ as a measure of the range of the ACF. The quantity X reflects the contrast of the ACF and is especially critical for proper weighting of the phase ACFs, since on many triangles ACF_ϕ is approximately constant though with small periodic peaks (Figure 9). Effectively, X/ξ quantifies the significance of a peak in the ACF. In practice, X is frequently small for ACF_ϕ on certain triangles, although the very high S/N of the closure phases on the small SMTO–CARMA–LMT and Hawaii–SMTO–CARMA triangles (which do not resolve out much of the total flux) often compensates by producing a very clean ACF (i.e., ξ is small as well). In order to identify the period in an algorithmic way, we created a "folded" version of the composite array ACF, defined as

$$\mathrm{Fold}(k) \equiv \frac{1}{\lfloor m/k \rfloor} \sum_{i=1}^{\lfloor m/k \rfloor} \mathrm{ACF}(i \cdot k), \qquad (12)$$

where m is the number of points in the ACF. Folding the ACF effectively suppresses the trivial peak at zero lag. In the absence of noise, the peak of Fold(k) is the period.

In order to test for the significance of periodicity detection, we ran Monte Carlo simulations for each model and array at bit rates from 1 to 32 Gbit s^{-1} by powers of two. We ran 10,000 simulations of the data with different noise instantiations and obtained the value of k maximizing Fold(k). The distribution of Fold(k) provides information on the probability of false detection of periodicity. The results are summarized in Table 3, which lists the number of trials for which max(Fold(k)) misidentifies the period, rounded to the nearest 10 s, by more than one minute. Four and a half orbital periods of simulated data were used, corresponding to 2 hr for Models A-D and 37 minute for Model E.

It is clear that the inclusion of a fourth or fifth telescope in the western hemisphere array produces a large improvement in periodicity detectability. This is due both to the much larger number of closure quantities that can be averaged together to produce a detection and also to the fact that a four- or five-element array will necessarily probe a larger range of spatial scales than possible three-element arrays, which is important because it is not clear a priori which triangle will be best matched to the angular resolution of the variable emission in Sgr A*. Additional bandwidth is important as well, but less so than additional telescopes in the observing array. The Hawaii–SMTO–CARMA array, for example, is insensitive to periodic structure in several models, even at high recording rates. But inclusion of a Chilean telescope, and/or the LMT, produces a robust detection of periodicity at modest recording rates. It is especially worth noting that a bit rate of 8 Gbit s^{-1}, corresponding to 2 GHz total bandwidth (e.g., 1 GHz in each of two orthogonal polarizations) is sufficient to produce clear periodicity detections (with error rate $< 1 \times 10^{-4}$) in nearly all models provided that at least four telescopes are used in the array. For the Europe–Chile triangle, where no clear fourth telescope is presently available, the use of high bit rates and phased ALMA will be critical for periodicity detection.

Array options at 345 GHz are relatively limited, since neither the LMT nor PV have planned 345 GHz capability. We include the Europe–Chile triangle to show what might be expected if PV is ever upgraded to include a 345 GHz receiver. The largest simultaneous array that can be deployed at 345 GHz in the near future consists of the three US telescopes and a Chilean station. Should phased ALMA not become available, an array consisting of Hawaii, SMTO, CARMA, Chile-1, and the LMT with a 345 GHz receiver (but not otherwise optimized for 345 GHz performance) would suffice to detect periodicity in Models A–E at bit rates of 2 Gbit s^{-1} or higher.

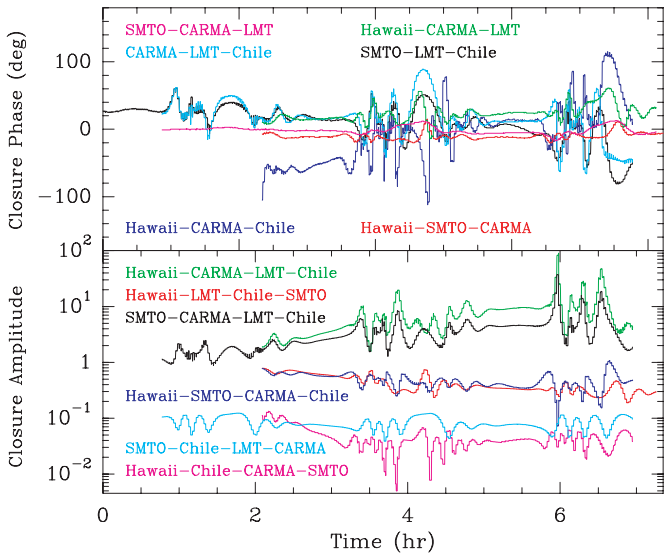

Figure 10. Closure phases and amplitudes for Model F at 230 GHz (period 2.8 hr). The colored lines indicate the closure quantities that would be obtained in the absence of noise. The abscissa shows the time range over which Sgr A* is above 5° elevation at least three western hemisphere telescopes. Due to changing baseline orientations, closure phases and amplitudes do not approximately repeat, although significant deviations are seen simultaneously on most subarrays. Very small spikes seen in some of the lines are artifacts of the modeling.

Observations have recently been taken with an array consisting of the JCMT, SMTO, and CARMA-1 at 230 GHz (Doeleman et al. 2008). We run simulations of this array, which is usable already, as well as the same three telescopes with the addition of Chile-1, since APEX is likely to have 230 GHz capability in the near future. We find that periodicity may be just marginally detectable at the current maximum bit rate of 4 Gbit s^{-1} if the source geometry in Sgr A* is favorable. Larger bandwidths are critical for detecting periodicity on these arrays (and may not suffice if only the US telescopes are used, depending on source geometry). It is likely that phased-array capability at Hawaii and CARMA will become available on the same timescale as higher bit rate capability. At 345 GHz, an array consisting of the JCMT, SMTO, and Chile-1 (APEX or ASTE) would not suffice to detect periodicity except at very high bit rates ($\geqslant$ 32 Gbit s^{-1}, depending on the model).

4.4. Long-Period Models

Detecting periodicity in the closure quantities will be more difficult if the hot spot orbital period is long (e.g., several hours). The change in baseline orientation is significant enough within the 167 minute orbital period in Model F that the closure quantities do not approximately repeat, as shown in Figure 10. Consequently, the corresponding ACFs on most triangles and quadrangles fall off with increasing lag, so the period cannot be determined by finding the largest peak in the ACF. Closure phases and amplitudes show periods of relative quiescence punctuated by periods of large simultaneous variability on most subarrays.

Table 3
Probabilities of False Periodicity Detection

Model	Period[a] (s)	Array	P_{32} ($\times 10^{-4}$)	P_{16} ($\times 10^{-4}$)	P_8 ($\times 10^{-4}$)	P_4 ($\times 10^{-4}$)	P_2 ($\times 10^{-4}$)	P_1 ($\times 10^{-4}$)
		230 GHz						
A	1620	JCMT, SMTO, CARMA-1	0	0	0	5	397	2199
		JCMT, SMTO, CARMA-1, Chile-1	0	0	0	0	27	978
		Hawaii, SMTO, CARMA	0	0	0	0	1	134
		Hawaii, SMTO, CARMA, Chile-1	0	0	0	0	0	0
		PV, PdB, Chile-1	0	51	655	2516	5542	8093
		PV, PdB, Chile-10	0	0	0	0	1	134
B	1620	JCMT, SMTO, CARMA-1	157	2216	6653	9126	9666	9566
		JCMT, SMTO, CARMA-1, Chile-1	0	12	111	517	2356	5696
		Hawaii, SMTO, CARMA	0	0	94	1827	6231	8981
		Hawaii, SMTO, CARMA, Chile-1	0	0	2	80	535	2119
		Hawaii, SMTO, CARMA, LMT, Chile-1	0	0	0	0	0	0
		PV, PdB, Chile-1	97	548	1138	2473	5003	7545
		PV, PdB, Chile-10	0	0	0	6	185	724
C	1620	JCMT, SMTO, CARMA-1	0	0	2	41	316	1426
		JCMT, SMTO, CARMA-1, Chile-1	0	0	0	0	5	369
		Hawaii, SMTO, CARMA	0	0	0	0	0	21
		Hawaii, SMTO, CARMA, Chile-1	0	0	0	0	0	0
		PV, PdB, Chile-1	180	1993	4694	6943	8357	9183
		PV, PdB, Chile-10	0	0	0	12	437	2759
D	1620	JCMT, SMTO, CARMA-1	9195	9679	9809	9854	9871	9883
		JCMT, SMTO, CARMA-1, Chile-1	0	0	3	553	4435	7702
		Hawaii, SMTO, CARMA	3689	7207	8981	9556	9770	9825
		Hawaii, SMTO, CARMA, Chile-1	0	0	0	3	754	5584
		Hawaii, SMTO, CARMA, LMT, Chile-1	0	0	0	0	0	0
		PV, PdB, Chile-1	6477	8667	9337	9562	9561	9593
		PV, PdB, Chile-10	0	1	349	3309	7389	8983
E	490	JCMT, SMTO, CARMA-1	2318	4953	6730	7557	7873	8098
		JCMT, SMTO, CARMA-1, Chile-1	0	0	70	991	3208	5240
		Hawaii, SMTO, CARMA	1	204	1753	4394	6385	7390
		Hawaii, SMTO, CARMA, Chile-1	0	0	0	34	772	3238
		Hawaii, SMTO, CARMA, LMT, Chile-1	0	0	0	0	0	7
		Hawaii, SMTO, CARMA, LMT, Chile-10	0	0	0	0	0	0
		PV, PdB, Chile-1	5987	6943	7461	7300	7037	7184
		PV, PdB, Chile-10	57	778	2564	4750	6454	7211
		345 GHz						
A	1620	Hawaii, SMTO, Chile-1	0	20	1488	6582	8890	9505
		Hawaii, SMTO, CARMA	0	0	0	11	395	2588
		Hawaii, SMTO, CARMA, Chile-1	0	0	0	0	90	1062
		Hawaii, SMTO, CARMA, Chile-10	0	0	0	0	0	0
		PV, PdB, Chile-10	0	0	0	0	0	26
B	1620	Hawaii, SMTO, Chile-1	0	0	45	2276	7064	9076
		Hawaii, SMTO, CARMA	4	424	4718	8504	9541	9785
		Hawaii, SMTO, CARMA, Chile-1	0	0	0	126	2676	7086
		Hawaii, SMTO, CARMA, Chile-10	0	0	0	0	0	0
		PV, PdB, Chile-10	0	0	5	767	5066	8194
C	1620	Hawaii, SMTO, Chile-1	0	0	1	366	4675	8560
		Hawaii, SMTO, CARMA	0	0	0	1	71	1210
		Hawaii, SMTO, CARMA, Chile-1	0	0	0	0	2	161
		Hawaii, SMTO, CARMA, Chile-10	0	0	0	0	0	0
		PV, PdB, Chile-10	0	0	0	43	2154	7393
D	1620	Hawaii, SMTO, Chile-1	0	0	137	3147	7632	9110
		Hawaii, SMTO, CARMA	0	0	8	582	3582	6901
		Hawaii, SMTO, CARMA, Chile-1	0	0	0	19	1933	6664
		Hawaii, SMTO, CARMA, Chile-10	0	0	0	0	0	0
		PV, PdB, Chile-10	0	0	73	2183	6871	8590
E	490	Hawaii, SMTO, Chile-1	105	1057	2453	3554	4307	5617
		Hawaii, SMTO, CARMA	0	3	192	1705	4099	5838
		Hawaii, SMTO, CARMA, Chile-1	0	0	61	924	2112	3137
		Hawaii, SMTO, CARMA, Chile-10	0	0	0	0	0	5
		PV, PdB, Chile-10	34	890	3183	5088	6093	6466

Notes. Right columns indicate probabilities of false period identifications (more than 60 s from true period) in 10,000 trial runs at subscripted bit rate in Gbit s^{-1}. Arrays are not listed when a listed proper subset of the array produces no false detections at 1 Gbit s^{-1} (e.g., Hawaii, SMTO, CARMA, [LMT], Chile-10 in Model A at 230 GHz).

[a] Rounded to nearest 10 s.

The mutual visibility on most triangles and quadrangles is comparable to twice the orbital period of the long-period models, so periodic behavior in closure phases and amplitudes may not be convincing in demonstrating source structure periodicity. For instance, it may not be clear whether closure phases and amplitudes such as those shown in Figure 10 are due to a hot spot in a large orbit or due to two unrelated flaring episodes of an aperiodic nature. The LMT may be critical for establishing long-period periodicity, since its inclusion lengthens the total time range for observing, increasing the chance that a third period will be detected. While present millimeter-VLBI arrays are thus not optimal for detecting long-period orbiting hot spots, observational evidence suggests that hot spot periods may be significantly shorter than that in Model F. VLBI measurements of the position of the centroid of emission from Sgr A* presently constrain the orbital period of hot spots to be $\lesssim 120$ minute if the hot spot flux dominates the disk flux, with progressively longer periods allowed as the hot spot-to-disk flux ratio decreases (Reid et al. 2008).

However, there are fundamental constraints upon the existence of such long-period hot spots. The synchrotron cooling time at millimeter wavelengths is roughly 3 hr (see Equation (4)), and thus in the absence of a continuous mechanism for injecting energetic electrons in the hot spot, we would not expect to see single hot spots persist longer than this. Additionally, the available energy (magnetic & hydrodynamic) that may be tapped to generate substantial emission decreases rapidly with radius, implying that the brightest (and therefore dominant) events will preferentially occur at small radii, with correspondingly short dynamical timescales.

5. DISCUSSION

5.1. Observing Strategies and Telescope Prioritization

Ultimately, observations are limited by the telescopes that are available. Individual observers often have little influence over telescope construction priorities. Nevertheless, it is important to consider the relative advantages of planned and potential instruments. Future observers may be limited by scarce resources, such as DBEs and recording equipment, instead of by available telescopes.

Array phasing will be crucial for maximizing the potential of millimeter VLBI arrays. Phased versions of CARMA and the millimeter telescopes on Mauna Kea are necessary in order to increase the detectability of very weak signals on the long baselines. However, further observations on the Hawaii–CARMA–SMTO triangle should not be deferred due to the lack of a phased-array processor at Hawaii and/or CARMA. In some models, periodicity could be detected on the triangle consisting of the JCMT, a single CARMA dish, and the SMTO at high bandwidth. Most of our models also indicate that periodicity may be detectable on the Hawaii–CARMA–Chile-1 triangle, although the use of phased ALMA rather than a single dish as the Chilean telescope may also be important for detecting periodicity if the black hole is highly rotating or if hot spot flux density signatures are typically smaller than assumed in this work.

Given the schedule of proposed telescope upgrades, observations utilizing closure techniques in the near future are most likely to use the Hawaii–CARMA–SMTO triangle at 230 GHz and the Hawaii–SMTO–Chile triangle at 345 GHz, with the possibility that the JCMT and/or CARMA-1 may necessarily be used in place of Hawaii and CARMA for the earliest observations. As illustrated in Figure 5 (and Table 3), the Hawaii–CARMA–SMTO triangle at 230 GHz may not provide adequate spatial resolution to detect an orbiting hot spot, depending on the parameters of the Sgr A* system. At the other extreme, the currently available array of Hawaii, SMTO, and Chile-1 at 345 GHz may resolve out most of the emission (Figure 4) and is unlikely to be useful for periodicity detection by itself at data rates less than about 16 Gbit s^{-1}. We therefore conclude that observations of Sgr A* in the near future to detect periodicity should be taken at 230 GHz.

It will be important to include a fourth antenna in the array at each frequency. As demonstrated in Section 4.2, the additional closure phases and amplitudes obtained by a four-element array may be important for detecting periodicity. Even if periodicity can be marginally detected by a three-element array, the extra four independent-closure quantities provided by inclusion of a fourth telescope will vastly increase the significance of periodicity detection. Early observations at 230 GHz should include APEX or a single ALMA dish, if at all possible, in order to provide a fourth station in the array (otherwise assumed to include Hawaii, SMTO, and CARMA). A key benefit of a four-station US-Chile array, beyond the much larger number of closure quantities provided, is that the constituent baselines will be sensitive to a large range of spatial scales, making it less likely that periodicity will be missed due to a mismatch between the angular scale of source structure variability and the angular resolution of the array.

The LMT will be a critical telescope for two reasons. First, it fills in an important hole in the (u, v) plane, allowing for a large range of angular scales to be probed by the full array. Indeed, the LMT produces excellent closure phase data on some triangles for every model considered in this work. Second, inclusion of the LMT allows for simultaneous visibility of Sgr A* from up to five telescopes. The utility of the LMT derives especially from its location and its size. Even an incomplete LMT (e.g., a 32 m dish, as assumed in this work) whose surface has not yet been fully tuned to maximize aperture efficiency would be highly useful for observations of the Galactic center at 230 GHz. Thus, we conclude that millimeter wavelength VLBI arrays observing Sgr A* should include the LMT as soon as is practical.

There is also a need for 345 GHz capability at a greater number of telescopes. CARMA would be especially useful due both to its large effective collecting area as well as its short baselines to the SMTO and Hawaii. The same comments that apply to the LMT in its planned 230 GHz band also apply to a future 345 GHz system, if ever planned. Expanding PV to include 345 GHz would allow for observations on the Europe–Chile triangle, which would provide only one additional closure phase and is therefore not a high priority for periodicity detection. However, the long Europe–Chile baselines cover an otherwise unsampled region of the (u, v) plane and may therefore prove to be important for eventual modeling of the Sgr A* quiescent disk.

An alternative observing strategy for the Chilean site, if phased ALMA is unavailable, would be to use multiple individual telescopes. Baselines from the Chilean telescopes (APEX, ASTE, or a single ALMA dish) to North American or European telescopes would effectively be redundant with each other in the (u, v) plane but would offer independent data, thus increasing the number of closure quantities available. Baselines between Chilean telescopes would be too short to resolve the emission from Sgr A* but would provide a valuable simultane-

ous (near-)zero-spacing flux measurement, allowing estimation of the fraction of flux resolved out by the short PV–PdB or SMTO–CARMA baselines.

5.2. Bandwidth Considerations

Our simulations indicate that the periodicity of reasonable hot spot models is detectable on most millimeter VLBI triangles/quadrangles at data rates from 1 to 32 Gbit s^{-1}. However, we note several caveats whose applicability depends on the exact physical parameters of the Sgr A* system. It may be difficult to detect periodicity on the smallest triangles due to insufficient spatial resolution. Conversely, the largest triangles may resolve out much of the emission. Very high data rates may be required to detect periodicity on long triangles to Chile-1. During any particular track of observations, it is possible that no hot spot will be present, or that the flux density of the hot spot may be substantially smaller than assumed here.

We have assumed throughout that the atmospheric coherence time is 10 s. In poorer weather conditions, the coherence time may be significantly shorter. Since the S/N of a coherently integrated visibility grows as $(Bt)^{1/2}$, where B is the bandwidth, the S/N for a single visibility integrated over a 2.5 s coherent time interval will be half that of a visibility integrated over 10 s. So long as the signal is strong enough compared to the noise (i.e., the S/N $\gg 1$ in a single coherent integration), there is no net loss of signal because the decrease in S/N is exactly compensated by the increase in the number of data points obtained. The S/N of the closure phase can then be built up over a longer period of time, if desired, by averaging consecutive closure phases (provided that the noiseless closure phase is not changing rapidly over the timescale of integration). Periodicity may still be weakly detected if the average S/N exceeds unity over only a portion of the hot spot orbit, as could be the case if the visibility amplitude on the weakest baseline changes by a factor of several over an orbit.

Due to this effective S/N cutoff, it will be important to obtain data at the maximum bandwidth (or recording rate) possible at the time of observations. Initial observations may be bandwidth limited to 1 GHz (4 Gbit s^{-1}). If subsequent observations are limited by average recording rate rather than IF bandwidth, it will be advantageous to use burst-mode recording, if available. In the limit of marginal detections, it is far preferable to have a reduced number of good data points rather than a full set of poor data.

5.3. Black Hole Parameter Estimation

The observation of periodicity in the closure quantities would provide important evidence, independent of observations of periodicity in flare light curves, that at least some subset of Sgr A*'s flares are due to bright orbiting structures. This is critical to efforts to use such structures (e.g., hot spots) to infer the properties of the black hole spacetime.

In principle, combined with the flare amplitude (as measured via the unresolved light curves), the degree of variability in the closure quantities is indicative of the size of the hot spot orbit. Combined with the period, this provides a straightforward way in which to estimate the spin. However, the precision with which submillimeter closure quantities can constrain the spin has yet to be determined, and will likely have to await a detailed parameter-space study. On the topic of black hole spin, it should be pointed out that arguments for a nonzero spin of the SgrA* black hole can be made based on the observed intrinsic size of Sgr A* at 1.3 mm (Doeleman et al. 2008), and from NIR variability results (Genzel et al. 2003).

Our methods are generalizable to any mechanism of flare production. There will almost surely be asymmetric structure on scales of a few to a few tens of R_S due to general relativistic effects from the accretion disk. Regardless of whether flares are produced by orbiting or spiraling hot spots, jets, magnetohydrodynamic instabilities, or some other mechanism, there will also be asymmetric structures in the inner disk region on scales of a few R_S. Our models demonstrate that millimeter wavelength VLBI arrays will be sensitive to changes in the source structure no matter how these asymmetries are oriented relative to each other on the sky.

5.4. Summary of Simulation Findings

1. The currently useable 230 GHz array consisting of SMTO, CARMA-1, and JCMT at 4 Gbit s^{-1} cannot detect periodicity in any of the models tested.
2. Phasing connected element arrays (CARMA, Hawaiian telescopes, ALMA) to form large effective apertures, significantly improves the probability of detecting the hot spot period. When the CARMA array is phased, and the Hawaiian telescopes are coherently summed, periodicity in two out of five of the 230 GHz models can be detected. When 10 elements of ALMA are phased together, periodicity can be reliably extracted in all of the 230 GHz models tested.
3. Higher recording bandwidth increases S/N on all baselines, thereby improving periodicity detection, and making the array more robust against loss of VLBI signal coherence due to atmospheric turbulence. In three out of five 230 GHz models tested, a recording bandwidth of 16 Gbit s^{-1} allows detection of periodicity using just a three-station VLBI array.
4. Adding a fourth or fifth telescope to the array enables detection of the hot spot period *in every* 230 GHz model tested. The added baseline coverage in larger arrays allows more complete sampling of spatial scales in SgrA*.
5. Inclusion of the LMT in 230 GHz arrays will be very important as baselines to the LMT fill critical voids in baseline coverage. When long baselines between the US and Chile heavily resolve SgrA*, baselines between each of these regions and the LMT can still provide high S/N detections that connect all telescopes in the array.
6. A 345 GHz capability at more sites is needed. The currently available 345 GHz array, consisting of SMTO, Hawaii, and Chile has long baselines that will resolve much of the flux density of SgrA*. Enhancing either CARMA or the LMT with low-noise 345 GHz receivers, puts periodicity detection of all the tested 345 GHz models within reach when ALMA comes on line.

5.5. Conclusions

Motivated by recent detection of intrinsic structure within SgrA* on $< 4R_S$ scales, this work explores the feasibility of detecting time-variable structure and periodicity in the context of flare models in which a hot spot orbits the central black hole. Algorithms are described that use interferometric closure quantities, direct VLBI observables which reflect asymmetries in source structure that can be tracked on timescales that are short compared to presumed hot spot orbital periods. We find that periodicity from these models over a representative range of parameters can be reliably extracted using millimeter and

submillimeter VLBI arrays that are planned over the next five years. Thus, millimeter and submillimeter VLBI has matured to the level where one can envisage studying fundamental black hole parameters, accretion physics, and General Relativity in the strong field regime at meaningful angular resolutions.

The techniques and concepts described here are applicable to a broad range of Sgr A* models, including emission due to jets and outflows, MHD simulations, and adiabatically expanding flaring structures. Closure amplitude analysis, for example, is capable of tracking the size of SgrA* over time and sensitively testing for expansion during a flare event. Short wavelength VLBI, when coupled with wide spectrum simultaneous monitoring, can thus make detailed tests of emission models for Sgr A* in which low-frequency synchrotron photons are upscattered to produce X-rays.

The three fundamental technical efforts to improve millimeter and submillimeter arrays include increasing the number of VLBI sites, achieving the capability to phase connected element arrays into a large effective aperture, and increasing the VLBI recording data rate. Projects in each of these areas, supported by an international collaboration, are underway, and it is expected that observations on VLBI arrays at 1.3 mm and 0.85 mm wavelength with dramatically improved sensitivities will begin by 2009. The increase of bandwidth, while of general importance to lowering VLBI detection thresholds, may be most useful by enabling full polarization observations. The techniques developed in this work can be extended to nonimaging VLBI polarimetry analysis, allowing tests for small scale polarization structure to be carried out. The prospect of using VLBI to probe such polarized substructure emphasizes the power of the technique for studying Sgr A*.

The high-frequency VLBI program at Haystack Observatory is funded through a grant from the National Science Foundation.

REFERENCES

Agol, E. 2000, ApJ, 538, L121
Aitken, D. K., et al. 2000, ApJ, 534, L173
Aschenbach, B., Grosso, N., Porquet, D., & Predehl, P. 2004, A&A, 417, 71
Backer, D. C. 1978, ApJ, 222, L9
Backer, D. C., & Sramek, R. A. 1999, ApJ, 524, 805
Baganoff, F. K., et al. 2001, Nature, 413, 45
Bélanger, G., Terrier, R., de Jager, O. C., Goldwurm, A., & Melia, F. 2006, J. Phys. Conf. Ser., 54, 420
Blandford, R. D., & Begelman, M. C. 1999, MNRAS, 303, L1
Bower, G. C., Falcke, H., Herrnstein, R. M., Zhao, J.-H., Goss, W. M., & Backer, D. C. 2004, Science, 304, 704
Bower, G. C., Goss, W. M., Falcke, H., Backer, D. C., & Lithwick, Y. 2006, ApJ, 648, L127
Bower, G. C., Wright, M. C. H., Falcke, H., & Backer, D. C. 2001, ApJ, 555, 103
Bower, G. C., Wright, M. C. H., Falcke, H., & Backer, D. C. 2003, ApJ, 588, 331
Broderick, A., & Blandford, R. 2003, MNRAS, 342, 1280
Broderick, A., & Blandford, R. 2004, MNRAS, 349, 994
Broderick, A. E. 2006, MNRAS, 366, L10
Broderick, A. E., & Loeb, A. 2005, MNRAS, 363, 353
Broderick, A. E., & Loeb, A. 2006a, ApJ, 636, L109
Broderick, A. E., & Loeb, A. 2006b, MNRAS, 367, 905
Bromley, B. C., Melia, F., & Liu, S. 2001, ApJ, 555, L83
Cornwell, T. J., & Wilkinson, P. N. 1981, MNRAS, 196, 1067
Doeleman, S., et al. 2002, in Proc. 6th European VLBI Network Symp., New Developments in VLBI Science and Technology, ed. E. Ros, R. W. Porcas, A. P. Lobanov, & J. A. Zensus (Bonn: Max-Planck Institut für Radioastronomie), 223
Doeleman, S. S., et al. 2001, AJ, 121, 2610
Doeleman, S. S., et al. 2008, Nature, 455, 78
Eckart, A., Schödel, R., Meyer, L., Trippe, S., Ott, T., & Genzel, R. 2006, A&A, 455, 1
Eckart, A., et al. 2004, A&A, 427, 1
Falanga, M., Melia, F., Tagger, M., Goldwurm, A., & Bélanger, G. 2007, ApJ, 662, L15
Falcke, H., & Markoff, S. 2000, A&A, 362, 113
Falcke, H., Melia, F., & Agol, E. 2000, ApJ, 528, L13
Genzel, R., Schödel, R., Ott, T., Eckart, A., Alexander, T., Lacombe, F., Rouan, D., & Aschenbach, B. 2003, Nature, 425, 934
Ghez, A., et al. 2008, ApJ, 689, 1044
Ghez, A. M., et al. 2003, ApJ, 586, L127
Ghez, A. M., et al. 2004, ApJ, 601, L159
Gillessen, S., et al. 2009, ApJ, 692, 1075
Goldston, J. E., Quataert, E., & Igumenschev, I. V. 2005, ApJ, 621, 785
Holdaway, M. A. 1997, MMA Memo Series No. 169
Hornstein, S. D., Matthews, K., Ghez, A. M., Lu, J. R., Morris, M., Becklin, E. E., Rafelski, M., & Baganoff, F. K. 2007, ApJ, 667, 900
Huang, L., Cai, M., Shen, Z.-Q., & Yuan, F. 2007, MNRAS, 379, 833
Jennison, R. C. 1958, MNRAS, 118, 276
Jones, T. W., & O'Dell, S. L. 1977, ApJ, 214, 522
Lindquist, R. W. 1966, Ann. Phys., 37, 487
Loeb, A., & Waxman, E. 2007, J. Cosmol. Astropart. Phys. JCAP03(2007)011
Macquart, J.-P., et al. 2006, ApJ, 646, 111
Maoz, E. 1998, ApJ, 494, L181
Markoff, S., Bower, G. C., & Falcke, H. 2007, MNRAS, 379, 1519
Marrone, D. P., Moran, J. M., Zhao, J.-H., & Rao, R. 2006, J. Phys. Conf. Ser., 54, 354
Marrone, D. P., Moran, J. M., Zhao, J.-H., & Rao, R. 2007, ApJ, 654, 57
Marrone, D. P., et al. 2008, ApJ, 682, 373
Melia, F., Bromley, B. C., Liu, S., & Walker, C. K. 2001, ApJ, 554, L37
Meyer, L., Do, T., Ghez, A., Morris, M. R., Witzel, G., Eckart, A., Belanger, G., & Schödel, R. 2008, ApJ, 688, L17
Meyer, L., Schödel, R., Eckart, A., Karas, V., Dovčiak, M., & Duschl, W. J. 2006, A&A, 458, L25
Miyoshi, M., Ishitsuka, J. K., Kameno, S., Shen, Z., & Horiuchi, S. 2004, Prog. Theor. Phys. Suppl., 155, 186
Monnier, J. D. 2007, New Astron. Rev., 51, 604
Narayan, R., Mahadevan, R., Grindlay, J. E., Popham, R. G., & Gammie, C. 1998, ApJ, 492, 554
Petrosian, V., & McTiernan, J. M. 1983, Phys. Fluids, 26, 3023
Quataert, E., & Gruzinov, A. 2000, ApJ, 545, 842
Reid, M. J. 1993, ARA&A, 31, 345
Reid, M. J., Broderick, A. E., Loeb, A., Honma, M., & Brunthaler, A. 2008, ApJ, 682, 1041
Reid, M. J., & Brunthaler, A. 2004, ApJ, 616, 872
Rogers, A. E. E., Doeleman, S. S., & Moran, J. M. 1995, AJ, 109, 1391
Rogers, A. E. E., et al. 1974, ApJ, 193, 293
Rogers, A. E. E., et al. 1994, ApJ, 434, L59
Shen, Z.-Q., Lo, K. Y., Liang, M.-C., Ho, P. T. P., & Zhao, J.-H. 2005, Nature, 438, 62
Tagger, M., & Melia, F. 2006, ApJ, 636, L33
Thompson, A. R., Moran, J. M., & Swenson, G. W., Jr. 2001, Interferometry and Synthesis in Radio Astronomy (New York: Wiley)
Trotter, A. S., Moran, J. M., & Rodríguez, L. F. 1998, ApJ, 493, 666
Twiss, R. Q., Carter, A. W. L., & Little, A. G. 1960, Observatory, 80, 153
Yuan, F., Markoff, S., & Falcke, H. 2002, A&A, 383, 854
Yuan, F., Quataert, E., & Narayan, R. 2003, ApJ, 598, 301
Yusef-Zadeh, F., Roberts, D., Wardle, M., Heinke, C. O., & Bower, G. C. 2006, ApJ, 650, 189